ARTICLES
https://doi.org/10.1038/s41560-017-0044-5
nature energy

Robust and conductive two-dimensional metal–organic frameworks with exceptionally high volumetric and areal capacitance

Dawei Feng[1], Ting Lei[1], Maria R. Lukatskaya[1], Jihye Park[1], Zhehao Huang[2], Minah Lee[1], Leo Shaw[1], Shucheng Chen[1], Andrey A. Yakovenko[3], Ambarish Kulkarni[4], Jianping Xiao[4], Kurt Fredrickson[4], Jeffrey B. Tok[1], Xiaodong Zou[2], Yi Cui[5] and Zhenan Bao[1]*

For miniaturized capacitive energy storage, volumetric and areal capacitances are more important metrics than gravimetric ones because of the constraints imposed by device volume and chip area. Typically used in commercial supercapacitors, porous carbons, although they provide a stable and reliable performance, lack volumetric performance because of their inherently low density and moderate capacitances. Here we report a high-performing electrode based on conductive hexaaminobenzene (HAB)-derived two-dimensional metal–organic frameworks (MOFs). In addition to possessing a high packing density and hierarchical porous structure, these MOFs also exhibit excellent chemical stability in both acidic and basic aqueous solutions, which is in sharp contrast to conventional MOFs. Submillimetre-thick pellets of HAB MOFs showed high volumetric capacitances up to 760 F cm^{-3} and high areal capacitances over 20 F cm^{-2}. Furthermore, the HAB MOF electrodes exhibited highly reversible redox behaviours and good cycling stability with a capacitance retention of 90% after 12,000 cycles. These promising results demonstrate the potential of using redox-active conductive MOFs in energy-storage applications.

Increasing demands for reliable and powerful energy sources continue to drive the development of new materials for energy-storage devices[1,2]. Electrochemical capacitors (ECs), also known as supercapacitors, represent an important class of energy-storage systems because they offer attractive parameters, such as an energy density much higher than that of electrolytic capacitors, fast charge/discharge capacities and excellent cycling lives that exceed tens of thousands of cycles[3]. However, further improvement in energy density is still needed to approach that of batteries to expand the usage of ECs to portable consumable electronics. Depending on the energy-storage mechanism, ECs can be classified into either electrical double-layer capacitors (EDLCs) or pseudocapacitors[3]. The capacitance of EDLCs stems from charge separation at the electrode/electrolyte interface and, therefore, is proportional to the surface area. Hence, high specific surface area (SSA) materials, for example, porous carbons, have been used[4,5]. Pseudocapacitive materials store charges via reversible redox reactions[3]. Transition metal oxides (TMOs) (for example, RuO_2 (ref. [6]), Nb_2O_5 (ref. [7]) and MnO_2 (ref. [6])) and conducting polymers (for example, polyaniline)[7] serve as typical examples. However, these materials are often high in cost and/or suffer from low cycling stability. Although new nanomaterials have been developed to address these issues, high capacitance can often only be achieved in submicrometre-thick thin films[8,9]. For practical applications, however, submillimetre-thick electrodes with high areal capacitance are desirable.

MOFs are porous materials with tunable structures and high surface areas[10]. Owing to the versatility in design and the accessibility of both inorganic and organic building blocks on the molecular level, MOFs have been identified as promising candidates for high-capacitance ECs[11–14]. However, the lack of electrical conductivity (σ) in most MOFs significantly limits the effective utilization of built-in redox centres, which results in a low capacitance and power density, and the weak chemical stability of these reported conductive MOFs has negative impacts on the long-term cycling performance[11,12,15,16].

Conductive MOF design generally follows established rules reported for coordination polymers, for example, coordination polymers with strong metal–ligand orbital hybridization can become semiconductors and conductors[17–21]. Compared with one-dimensional (1D) polymers, 2D and 3D MOFs possess high porosities and are able to allow the accessibility of their redox-active sites. However, when large ligands are used to construct 2D and 3D MOFs, the low intrinsic density of the framework limits the theoretical density of the redox-active sites and achievable gravimetric and volumetric capacitances. Recently, an intrinsically conductive MOF demonstrated a stable electrochemical performance[13]. The $Ni_3(HITP)_2$ MOF was found to have large pore sizes and a high SSA and was therefore an excellent candidate for double-layer capacitive energy storage. Indeed, electrical double layer (EDL) storage mechanism was observed to dominate but resulted in only moderate gravimetric (~100 F g^{-1}) and volumetric (~115 F cm^{-3}) capacitances. These values are on a par with some porous carbons, but do not outperform the optimal materials[13].

Herein we design a redox-active conductive MOF that benefits from the pseudocapacitive instead of the EDL charge-storage mechanism. To increase the density of redox active centres, we selected ultrasmall hexaaminobenzene (HAB) linker to construct conductive

[1]Department of Chemical Engineering, Stanford University, Stanford, CA, USA. [2]Berzelii Centre EXSELENT on Porous Materials, Department of Materials and Environmental Chemistry, Stockholm University, Stockholm, Sweden. [3]X-ray Science Division, Advanced Photon Source, Argonne National Laboratory, Argonne, IL, USA. [4]Department of Chemical Engineering, SUNCAT Center for Interface Science and Catalysis, Stanford University, Stanford, CA, USA. [5]Department of Materials Science and Engineering, Stanford University, Stanford, CA, USA. Dawei Feng, Ting Lei and Maria R. Lukatskaya contributed equally to this work. *e-mail: zbao@stanford.edu

MOFs. The HAB linker coordinates with d^8 and d^9 metal species that prefer square-planar coordination geometry, which leads to subnanometre pores. This ultimately yields highly dense frameworks (Fig. 1a) and exceptionally high volumetric and areal capacitance for submillimetre-thick ECs with our MOFs.

Preparation and structure determination

The HAB monomer was synthesized according to the literature[22], which was used as a building block for the synthesis of a 2D graphene-like structure[23]. After both systematic and extensive exploration of the synthetic conditions, HAB MOFs were obtained as black crystalline powders on reaction of the HAB linker and Ni(II) or Cu(II) salts in water in the presence of a base and with exposure to ambient air (Fig. 1b). X-ray photoelectron spectroscopy (XPS) and electron paramagnetic resonance (EPR) analyses of the Ni-HAB and Cu-HAB samples indicate that only N, C, and O peaks exist in addition to only one type of metal: Ni(II) and Cu(II) respectively (Supplementary Figs. 1–3). We observed that when the reaction was carried out without oxygen, no MOF was formed, which suggests the participation of O_2 in the MOF formation. Meanwhile, without the addition of the base, an oxidized product of HAB was obtained instead (Supplementary Fig. 4). In addition, we successfully isolated an intermediate product of Cu-HAB under anaerobic conditions in the absence of base. Ultraviolet–visible spectroscopy (UV–vis), infrared spectroscopy and powder X-ray diffraction (PXRD) all indicate that the metal-coordinated intermediate can be transformed further into the final product on the addition of base and exposure to oxygen (Supplementary Figs. 5 and 6). Therefore, we hypothesized that the formation of the HAB MOFs proceeds in three successive steps: (1) metal coordination with the HAB ligand, (2) deprotonation of $-NH_2$ on HAB by the base and (3) oxidation of the deprotonated HAB (Supplementary Fig. 7).

As shown in Fig. 1a, a 2D honeycomb layered structure is expected for the HAB MOFs because of the topological combination between the tritopic (hexadentate) HAB and the square planar coordinated Ni(II) and Cu(II). To investigate this further, we first used a molecular fragment of Ni/Cu-HAB to generate the model structure using density functional theory (DFT) calculations. The Ni-HAB fragment showed a potential cell parameter of $a=b=13.33$ Å (Supplementary Fig. 8) and the Cu-HAB fragment showed a potential cell parameter of $a=b=13.75$ Å. Next, our obtained high-resolution synchrotron PXRD showed an expected hexagonal pattern with unit cell parameters of $a=b=13.11$ Å for Ni-HAB (13.15 Å for Cu-HAB) and an interlayer spacing of 3.22 Å for Ni-HAB (3.19 Å for Cu-HAB) (Fig. 1b, Supplementary Tables 1 and 2). These experimental data are in good agreement with the fragment modelling results.

To ascertain the packing mode, three possible structural models were subsequently proposed: (1) an eclipsed model (space group *P6/mmm*), (2) a parallel-displaced model (space group *Cmcm*) and (3) a staggered model (space group $P6_3/mmc$) (Supplementary Figs. 9–15). DFT optimization was used for the eclipsed model to optimize the atom coordinates by confining the unit-cell parameters to the experimental values. The parallel-displaced and staggered models were then generated by translating the middle layer of the eclipsed model. These models were used for subsequent PXRD simulation and structure refinement (Supplementary Figs. 16 and 17). The electron-diffraction patterns of Cu-HAB agree well with the simulated diffraction pattern of the eclipsed model, and the other

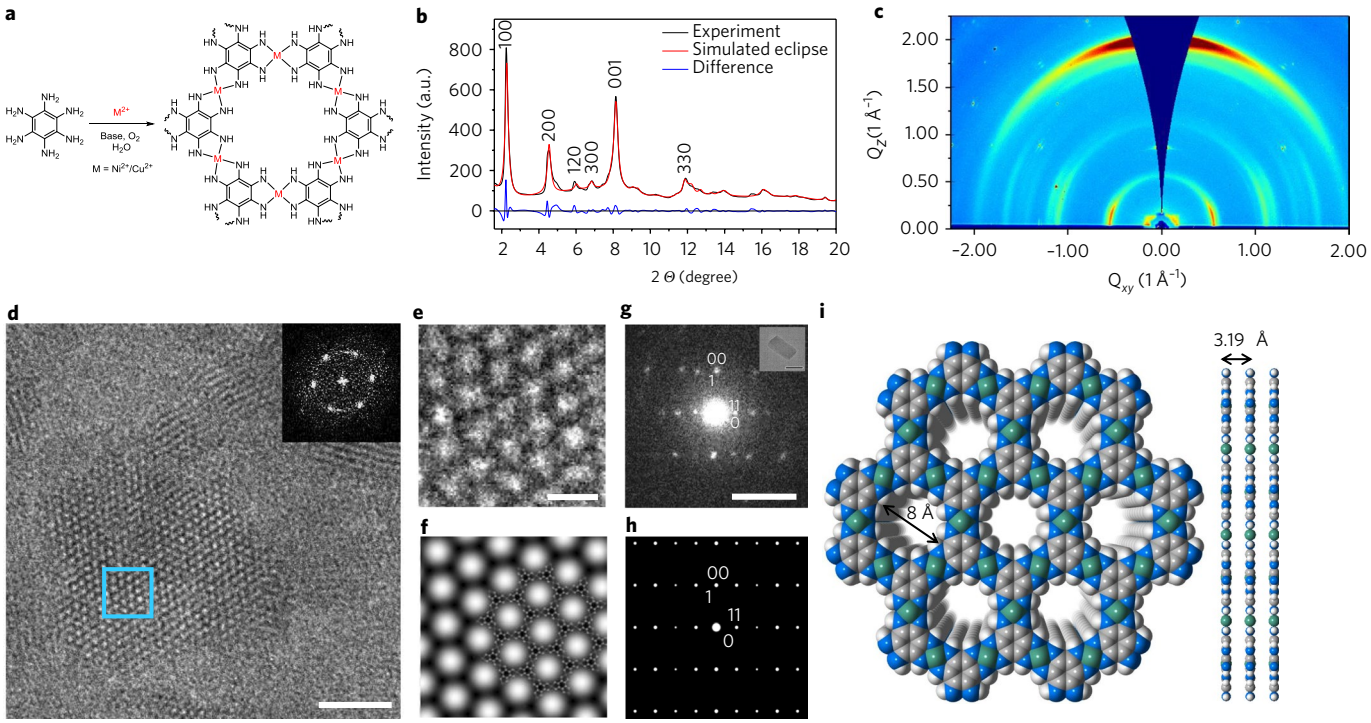

Fig. 1 | Synthesis and structural characterization of HAB MOFs. a, Synthesis scheme of Cu-/Ni-HAB MOFs. **b**, Experimental and Powley fitted PXRD patterns of Cu-HAB. **c**, 2D GIXD pattern of a Cu-HAB thin film on a Si substrate. **d**, HR-TEM image of Cu-HAB along [001] that shows a hexagonal pore packing with d_{100}=1.15 nm (a=1.33 nm). Scale bar, 10 nm. Inset: Fourier transform of the image. **e**, HR-TEM image of the region within the blue square in **d**. **f**, Symmetry-imposed and lattice-averaged image calculated from the HR-TEM image. Embedded is the eclipsed structure model of Cu-HAB. Scale bar, 2 nm. **g**,**h**, Experimental (**g**) and simulated (**h**) electron-diffraction pattern (eclipsed model) of Cu-HAB viewed along [−110]. Scale bar 5 nm^{-1}. Inset (**g**): the crystal from which the electron-diffraction pattern was taken. Scale bar, 50 nm. **i**, A space-filling model of the Cu-HAB model. Blue, grey, green and white spheres represent N, C, Ni and H atoms, respectively; a.u.: arbitrary units.

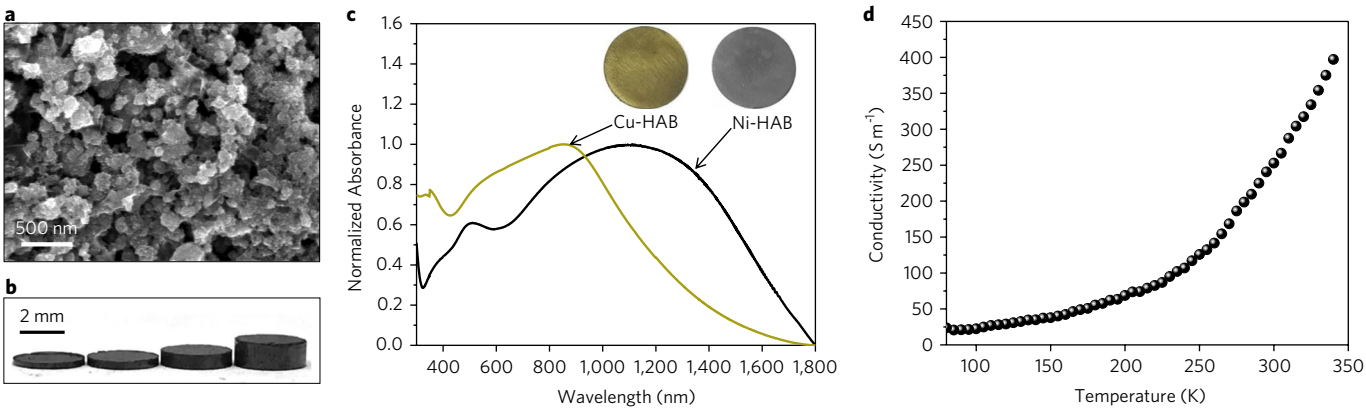

Fig. 2 | Preparation, absorption spectrum and conductivity of HAB MOFs pellets. a, SEM image of Ni-HAB powders. **b**, Ni-HAB pellets prepared by cold isostatic pressing. The diameter of the pellets is 3.18 mm, and the thicknesses from left to right are 0.20, 0.30, 0.59 and 1.07 mm. **c**, UV–vis–NIR absorptions of Ni-HAB and Cu-HAB films on a glass substrate. Inset: digital photographs of the HAB MOF pellets (pellet diameter, 12.7 mm). **d**, Temperature-dependent conductance of a Ni-HAB pellet.

two models can be excluded because they should present extra rows of reflections, which are not observed from our electron-diffraction results (Fig. 1g,h and Supplementary Fig. 11). The calculated d spacings of $d_{001}=3.24$ Å and $d_{010}=10.66$ Å correspond well with the eclipsed model ($d_{001}=3.19$ Å and $d_{010}=11.36$ Å). To confirm the structure further, a high-resolution transition electron microscopy (HR-TEM) image of the Cu-HAB MOF was obtained. The HR-TEM images (Fig. 1d–f and Supplementary Fig. 15) showed clear pores smaller than 1 nm with a honeycomb arrangement along [001] with $d_{100}=1.15$ nm. This observation strongly supports our proposed model because other structural models are either non-porous or contain much smaller pores. The 2D eclipsed model was further confirmed by N_2 adsorption isotherms. Both MOFs showed Brunauer–Emmett–Teller (BET) surface areas from ~180 $m^2 g^{-1}$ to 350 $m^2 g^{-1}$ based on different synthetic conditions, and micropores of ~0.8 nm (Supplementary Figs. 18 and 19), which correspond well with the calculated pore size from the eclipsed model (0.8 nm) (Supplementary Fig. 20).

To confirm the 2D structure further, we attempted to grow thin films of HAB MOFs. Through the control of the O_2 diffusion rate, highly reflective films were obtained on the water/air interface (Supplementary Figs. 21 and 22). Grazing-incidence X-ray diffraction (GIXD) of Cu-HAB films clearly revealed a predominantly face-on orientation of the 2D sheets. The (100) and (200) reflections primarily appeared in plane ($q_z \approx 0$), whereas the (001) peak is strong near the meridian ($q_{xy} \approx 0$), which indicates that the film consists mainly of 2D sheets oriented parallel to the substrate plane (Fig. 1c). Scanning electron microscopy (SEM) showed that HAB MOFs are aggregated small particles (Fig. 2a). Particle-size analysis of the obtained images indicated that the HAB MOFs have particle sizes in the range 5–50 nm, probably because of the rapid growth process of the MOFs, which contain highly stable coordination bonds with less reversibility (Supplementary Fig. 23). HAB MOF pellets with a tunable thickness can be obtained through cold isostatic pressing (Fig. 2b and Supplementary Fig. 24). They showed a high packing density of 1.77–1.80 g cm^{-3}, which is the highest among the reported MOFs with detectable porosity (Supplementary Table 3). The value is also close to the theoretical density of Ni-HAB as calculated from crystallographic data, possibly because of their small particle sizes as well as incomplete removal of the entrapped solvent molecules[24].

Optical and electrical properties

The π orbitals on the radical anionic HAB interact strongly with the d orbitals of Ni(II)/Cu(II), which enables a fully conjugated system. As expected, both HAB MOFs show a broad absorption band extending to the near-infrared region (Fig. 2c). Compressed pellets exhibit different colours depending on the metal centre: Cu-HAB is golden yellow and Ni-HAB is metallic grey (inset in Fig. 2c). From the onset of the absorption spectra, the bandgap of Ni-HAB is estimated to be ~0.57 eV, a value smaller than that of Cu-HAB (~0.74 eV). To characterize their electrical properties, the temperature dependence of conductivity was measured for the MOF pellets and shows a decent conductivity at low temperature (<100 K) (Fig. 2d). The Ni-HAB exhibited a higher conductivity of 70 ± 15 S m^{-1} at room temperature, whereas the Cu-HAB showed a lower conductivity of 11 ± 3 S m^{-1}. Furthermore, computational studies indicate that bulk Ni-HAB has a smaller band gap than bulk Cu-HAB, which is consistent with the absorption spectrum measurement (Supplementary Figs. 25–28). In addition, we found that the three-layer Ni-HAB is especially interesting as it showed Dirac cones, which implied a higher conductivity (Supplementary Fig. 26). Although a few MOFs have demonstrated high conductivities (for example, $Cu[Ni(pdt)_2]$, 10^{-2} S m^{-1} (pdt, 2,3-pyrazinditiolate); Cu-CAT-1, 20 S m^{-1}(CAT, catecholate); $Cu_3(HITP)_2$, 20 S m^{-1} (HITP, 2,3,6,7,10,11-hexaiminotriphenylen); $Ni_3(HITP)_2$, 5,000 S m^{-1}) (refs [13,20,25–27]), conductivity values obtained for our MOFs are, nonetheless, high and sufficient for the realization of conductive additive-free electrode design. Moreover, as the conductivity values were obtained for samples with an average particle size below 20 nm we envision that the conductivity of HAB MOFs can be improved further by optimizing the synthesis to yield larger crystallites[15].

Stability test

As HAB exhibits a strong orbital interaction with Ni(II)/Cu(II), the coordination bonds are highly robust against other reactive chemical species (for example, water and bases). Additionally, the hexadentate HAB, one of the smallest linkers, enables a significant 2D chelating effect to improve further both the thermodynamic and kinetic stabilities[28]. Consequently, these HAB MOFs demonstrated a good chemical stability in aqueous environments. For instance, the PXRD patterns and BET surface areas of MOFs treated in either saturated potassium hydroxide (KOH) (100 °C), saturated ammonium hydroxide (NH_4OH) (100 °C) or 1 M HCl did not show noticeable changes (Supplementary Fig. 29). To the best of our knowledge, this represents the largest pH stable range and the most basic environment that MOFs can withstand[28]. The excellent chemical stability of HAB MOFs allows for their use in low-cost and non-flammable aqueous electrolytes, whereas many traditional

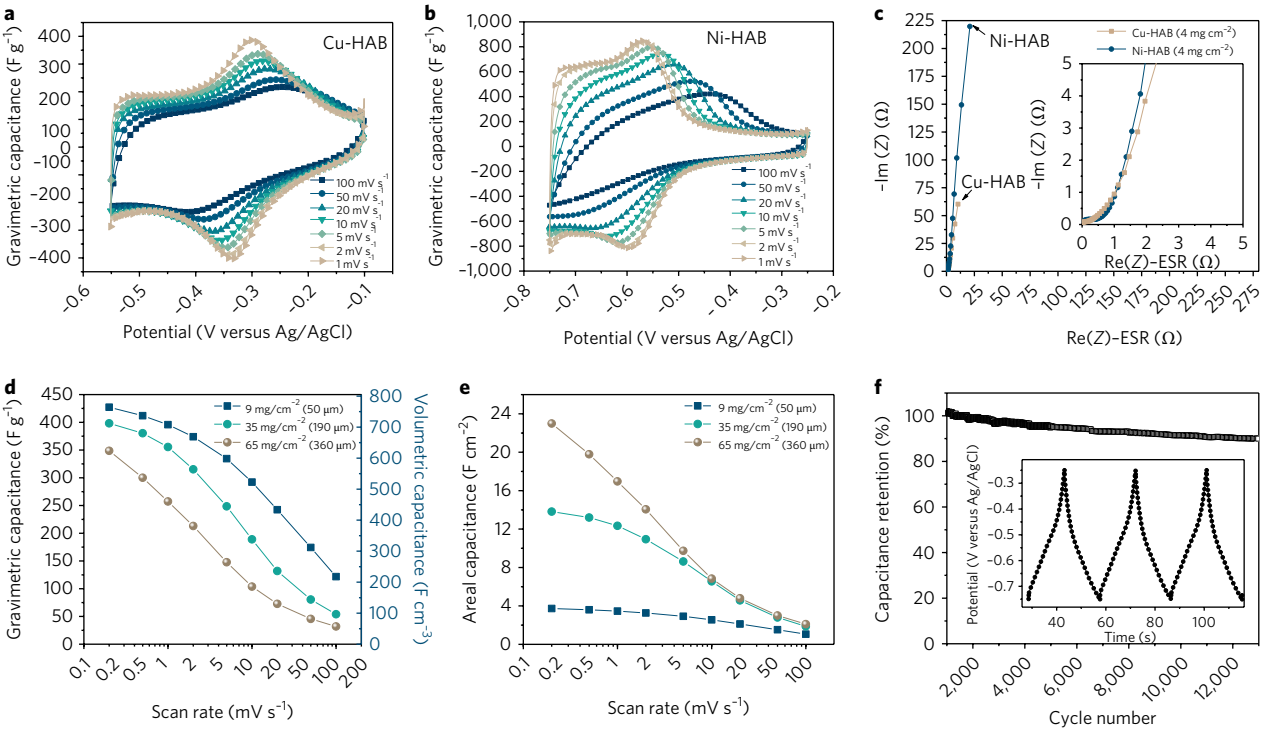

Fig. 3 | Electrochemical performance of HAB MOFs in 1 M KOH. a,**b**, Cyclic voltammetry profiles collected at different scan rates for Cu-HAB (**a**) and Ni-HAB (**b**) electrodes. **c**, EIS data collected for Cu-HAB Ni-HAB electrodes with weight loadings of 4 mg cm^{-2}. Inset: enlargement of high-frequency regions. Re(*Z*)–ESR represents the real part of the system impedance, in which the equivalent series resistance (ESR) was subtracted, and Im(*Z*) stands for the imaginary part of the system impedance. ESR, equivalent series resistance. **d**, Gravimetric and volumetric rate performance for Ni-HAB pellet electrodes with different areal densities of 9, 35 and 65 mg cm^{-2}. **e**, Areal rate performance for the Ni-HAB electrodes with different weight loadings. **f**, Capacitance retention data collected by galvanostatic charge discharge at 10 A g^{-1}. Inset: galvanostatic charge–discharge profiles.

MOFs are restricted to only organic electrolytes for ECs because of their weak chemical stability[13].

Electrochemical performance

The initial evaluation of the electrochemical performance was conducted in a traditional aqueous electrolyte, 1 M KOH, for both HAB MOF composite electrodes, that is, the electrodes were prepared with binder (5% polytetrafluoroethylene (PTFE)) and conductive additive (5% carbon black). The testing was carried out using an asymmetric three-electrode set-up with Ag/AgCl as the reference electrode and overcapacitive activated carbon as a counter electrode. Cyclic voltammetry studies revealed that the electrochemical behaviour of HAB MOFs is highly dependent on the metal centre, as distinctively different CV profiles were observed for Cu-HAB (Fig. 3a) and Ni-HAB (Fig. 3b). The Cu-HAB is characterized by CV profiles with a distinct peak at −0.315 V (1 mV s^{-1} scan rate), whereas the Ni-HAB has a substantially broadened peak region in the potential range from −0.5 V to −0.75 V. For both Ni-HAB and Cu-HAB at lower scan rates, the cyclic voltammetry profiles are characterized by an almost mirror image for the charge and discharge branches with a very small peak separation (at 1 mV s^{-1} the peak separation for Cu-HAB is 30 mV, whereas for Ni-HAB it is only 20 mV), which suggests a highly reversible electrochemical process, typical for classical pseudocapacitive materials[29], for example, Nb_2O_5 (ref. [30]), or the recently discovered 2D carbides, MXenes[31]. The presence of the clear redox peaks in the cyclic voltammograms for both HAB MOFs, along with the gravimetric capacitances of 420 F g^{-1} for Ni-HAB and 215 F g^{-1} for Cu-HAB, indicate a pseudocapacitance from reversible redox reactions being the dominant charge-storage mechanism in this highly conjugated system. The observed redox behaviour in HAB MOFs is most probably ligand based: (1) the HAB ligand shows a clear set of redox peaks as expected for the HAB-based family of molecules[32]; (2) the Ni and *o*-phenylenediamine (opda) coordination complex, Ni(opda)$_2$, which can be considered as non-porous analogue for Ni-HAB MOF because of the same structural motif (previously it was demonstrated that its redox activity is ligand based) and (3) the XPS of Ni^{2p} region before and after reduction showed no visible changes (Supplementary Discussion)[33].

We also performed an estimation of the EDL contribution to capacitance, which is <10% for Ni-HAB and <20% for Cu-HAB because of the moderate SSA of the HAB MOFs of 150–200 m^2 g^{-1} (Supplementary Discussion). This is most probably because of the substantial contribution of the redox charge-storage mechanism. Gravimetric capacitances achieved in the HAB MOFs, for example, Ni-HAB, are more than double those in the best currently reported porous carbon materials and close to those in redox-active conductive polymers and TMOs[3,34,35].

In regard to the rate-handling ability, the Cu-HAB retains 70% of its capacitance on increasing the scan rate from 1 to 100 mV s^{-1} (Supplementary Fig. 30a). For Ni-HAB, 65 % of the gravimetric capacitance of 420 F g^{-1} is maintained on a 100-fold scan rate increase from 1 mV s^{-1} (Supplementary Fig. 30b). Electrochemical impedance spectroscopy (EIS) for the HAB MOFs showed typical supercapacitor characteristics, that is, an almost vertical low-frequency region in the Nyquist plot with a low ionic resistance, which indicates an excellent accessibility of ions to active sites owing to the small HAB MOF particle size and intrinsic structural porosity (Fig. 3c).

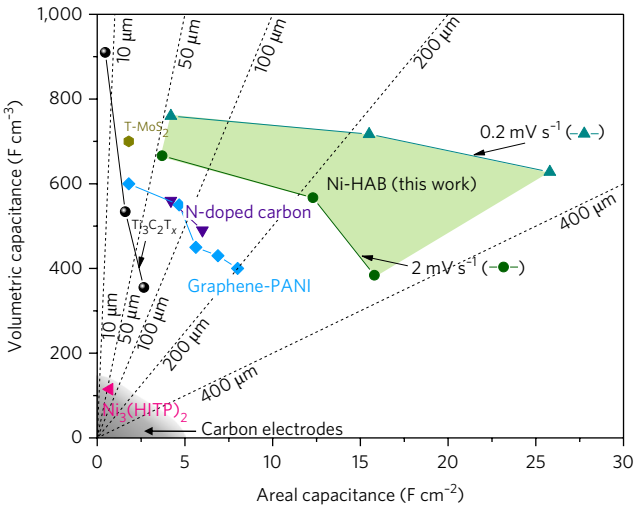

Fig. 4 | Comparison of the volumetric and areal capacitance of Ni-HAB additive-free electrodes (green area) with the performance of other materials. Those materials include $Ti_3C_2T_x$ (ref. [31]), holey graphene[4], $Ni_3(HITP)_2$ (ref. [13]), N-doped mesoporous carbon[36], graphene-PANI (PANI, polyaniline)[37], aMEGO-MnO_2 (aMEGO: activated microwave expanded graphite oxide) (ref. [6]), T-MoS_2 (T, T-phase) (ref. [38]) and porous carbon electrodes (shaded grey area)[8,16]. Dashed lines stand for guidelines of equivalent electrode thickness and shaded area represents the carbon electrodes.

Notably, the above tests were performed for electrodes with areal densities as high as 4 mg cm^{-2}, and therefore resulted in high areal capacitance values. For example, at 1 mV s^{-1}, capacitances of 0.86 F cm^{-2} and 1.6 F cm^{-2} can readily be achieved for Cu-HAB and the Ni-HAB composite electrodes, respectively. These values rival the best performing carbon/TMO electrodes (which have already been extensively optimized)[8].

For portable and miniature devices, both volumetric and areal performances are even more important metrics than gravimetric capacitance[4]. Hence, we further optimized Ni-HAB for better volumetric and areal performances. For that, we first prepared free-standing additive-free Ni-HAB pellets of different thicknesses and mass loadings. One of the important advantages of our prepared pellets is their high volumetric density of ~1.8 g cm^{-3}, which makes the volumetric performance of the Ni-HAB MOFs as high as 760 F cm^{-3} for a 50 μm thick pellet (areal density of 9 mg cm^{-2}, 427 F g^{-1} at 0.2 mV s^{-1} (Fig. 3d, Supplementary Fig. 31 and Supplementary Table 4)) and as high as 710 F cm^{-3} even for a 190 μm thick pellet (35 mg cm^{-2}; 400 F g^{-1} at 0.2 mV s^{-1}) with an areal capacitance of 13.7 F cm^{-2} (Fig. 3e and Supplementary Table 4). These obtained volumetric capacitance values are exceptionally high for electrodes of submillimetre thickness, and easily outperform the current best-known reported carbon electrodes[4,16,36,39], as well as thick electrodes of 2D carbides[31] (Fig. 4). On further increasing the pellet thickness to 360 μm, the volumetric capacitance at 1 mV s^{-1} was revealed as 460 F cm^{-3} and the areal performance was further improved to 23 F cm^{-2} (at 0.2 mV s^{-1}) and 17 F cm^{-2} (at 1 mV s^{-1}) (Fig. 3e and Supplementary Table 4). The areal capacitance is ~30 times higher than that of the recently reported conductive MOFs[13]. To the best of our knowledge, these recorded values are the highest in areal capacitance for additive-free electrodes (Fig. 4).

We hypothesized that our achieved high areal capacitance stems from two factors: (1) both the very small particle size of the Ni-HAB aggregates and the periodic porosity of the HAB MOFs enable easy access for the electrolyte and ions to the electrochemically active sites and (2) the intrinsic conductivity of the HAB MOFs proves to be sufficient to create conductive pathways for electrons within the pellet electrodes. Both these factors allow our usage of very thick electrodes without a plateauing of the areal capacitance. Moreover, our obtained capacitive performance of the Ni-HAB sample is well maintained with cycling, in which 90% of the capacitance was retained after 12,000 galvanostatic charge/discharge cycles performed at a current density of 10 A g^{-1} (Fig. 3f). The cycling stability correlates well with the absence of any substantial morphological changes in the MOF particles during the cycling processes, as observed by comparing the SEM images of pellet electrodes before and after 10,000 cycles (Supplementary Fig. 32).

Conclusions

We developed highly conductive 2D metal organic frameworks based on the HAB ligand and demonstrated that HAB-based MOFs have excellent chemical stability and therefore are compatible with aqueous electrolytes. We also highlight importance of the ligand selection in the conductive MOF design. In particular, the selection of the small HAB ligand not only allowed us to synthesize highly dense frameworks and tap into excellent capacitive volumetric performance, with exceptionally high volumetric capacitances up to 760 F cm^{-3}, superior to those of most materials (Fig. 4), but it also enabled us to achieve stable redox behaviour and gravimetric capacitance over 400 F g^{-1}. We established that, thanks to small HAB MOF particle size, even with an increase in electrode thickness up to 360 μm, the areal capacitance did not plateau and reached a value of over 20 F cm^{-2}. Moreover, the HAB MOF electrodes exhibited good cycling stability with a capacitance retention of 90% even after 12,000 cycles. We envision that the structure tunability and designability of MOFs will allow the further development of novel conductive MOFs with even higher capacitances for the next generation of energy-storage applications.

Methods

Ni-HAB powder synthesis. A solution of 80 mg (0.276 mmol) of nickel nitrate hexahydrate ($Ni(NO_3)_2{\cdot}6H_2O$) in 5 ml of water and 0.8 ml of concentrated aqueous NH_4OH was added to a solution of 30 mg (0.109 mmol) of HAB·3HCl in 5 ml of water. This mixture was stirred in an open beaker for 2 h at room temperature. The resulting black powder was centrifuged, filtered and then washed with water and 6 M NH_4OH at 100 °C. Finally, the solid was washed with acetone and dried under vacuum at 100 °C.

Cu-HAB powder synthesis. A solution of 70 mg (0.276 mmol) of copper nitrate hemi(pentahydrate) ($Cu(NO_3)_2{\cdot}2.5H_2O$) in 5 ml of water and 0.4 ml of concentrated aqueous NH_4OH was added to a solution of 30 mg (0.109 mmol) of HAB·3HCl in 5 ml of water. This mixture was stirred in an open beaker for 2 h at room temperature. The resulting black powder was centrifuged, filtered and then washed with water and 6 M NH_4OH at 100 °C. Finally, the solid was washed with acetone and dried under vacuum at 100 °C. Elemental analysis calculated for Cu-HAB ($CuC_4N_4H_4$): C, 27.99%; H, 2.35%; N, 37.02%; Cu, 32.64%; found: C, 22.77%; H, 2.24%; N, 23.85%; Cu, 32.92%.

Synthesis of the Ni-HAB film. A solution of 15 mg (0.052 mmol) of $Ni(NO_3)_2{\cdot}6H_2O$ in 8 ml of degassed water and 10 μl of ethylenediamine was mixed and added to a solution of 5 mg (0.109 mmol) of HAB·3HCl in 8 ml of degassed water in an O_2-free environment. The mixture was then transferred into a Petri dish and sealed with parafilm. The Petri dish was further sealed in a plastic container and transferred into the ambient environment. After 12 h, a silver thin film formed at the surface of the solution with a thickness of ~50 nm.

Synthesis of the Cu-HAB film. A solution of 15 mg (0.060 mmol) of $Cu(NO_3)_2{\cdot}2.5H_2O$) in 8 ml of degassed water and 50 μl of ethylenediamine was mixed and added to a solution of 5 mg (0.109 mmol) of HAB·3HCl in 8 ml of degassed water in an O_2-free environment. The mixture was then transferred into a Petri dish and sealed with parafilm. The Petri dish was further sealed in a plastic container and transferred into the ambient environment. After 12 h, a golden thin film formed at the surface of the solution with a thickness from 50 to 100 nm.

Characterizations. Continuous wave EPR measurements at the X band (9.4 GHz) were carried out at 120 K using a Bruker ELEXSYS E580 EPR

spectrometer equipped with an Oxford Instruments helium cryostat (ESR900) and a MercuryiTC temperature controller. The spectral simulations were performed using MATLAB 9.0.0.341360 (R2016a) and the EasySpin 5.1.5 toolbox. PXRD was carried out with a Bruker D8-Focus Bragg-Brentano X-ray Powder Diffractometer equipped with a Cu-sealed tube ($\lambda = 1.54178$ Å) at 40 kV and 40 mA. Synchrotron PXRD was carried out on 17-BM at the Advanced Photon Source ($\lambda = 0.45336$ Å) at the Argonne National Laboratory. GIXD was performed at the Stanford Synchrotron Radiation Lightsource (SSRL) at beamline 11-3 with a planar MAR CCD (charge-coupled device) detector. The incident angle was 0.20°, which probes the complete thickness of the film while avoiding multiple reflections that arise from the Si substrate with native oxide. The beam energy was 12.735 keV with a sample-to-detector distance of 300 mm. All the samples were kept in a helium environment to minimize air scattering, and the data were corrected to account for the planar detector. Absorption spectra were taken with a CARY 6000i UV–Vis–NIR spectrophotometer. Atomic force microscopy studies were performed with a Nanoscope VI Multimode microscope. All the experiments were carried out in tapping mode under ambient conditions. A silicon nitride cantilever with an Al coating was used with a resonant frequency around 300 kHz. Gas-adsorption measurements were made using a Micromeritics ASAP 2420 system at 77 K. Before the gas-sorption experiment, as-synthesized HAB MOF (~100 mg) samples were washed with NH_4OH (6 M) three times and then with water and acetone. Afterwards, the mixture was centrifuged, and then the acetone was removed by decanting. The samples were activated by drying under vacuum and then dried again by using the 'outgas' function of the adsorption instrument for 5 h at 100 °C prior to the gas adsorption/desorption measurement. The computational calculation of the accessible surface area of Cu/Ni-HAB MOF was carried out using the a literature method[40]. SEM observation was performed with a field emission-scanning electron microscope (JEOL JSM-7401F or Magellan 400 XHR) at 10.0 kV. To observe the genuine external surface, the samples were examined without any metal coating. Low-dose transmission electron microscopy (TEM) imaging was performed on a JEOL JEM2100 microscope operated at 200 kV (Cs 1.0 mm, point resolution 0.23 nm). Samples for TEM were dispersed in acetone. A droplet of the suspension was transferred onto a carbon-coated copper grid. Images were recorded with a Gatan Orius 833 CCD camera (resolution 2,048 × 2,048 pixels, pixel size 7.4 µm) under low-dose conditions[41]. Electron-diffraction patterns were recorded with a Timepix pixel detector QTPX-262k (512 × 512 pixels, pixel size 55 µm (Amsterdam Scientific Instruments).

Conductivity measurements. The pellets (20~40 um thick) for the conductivity measurement were prepared by cold isostatic pressing using commercial pressing equipment (MTI). The measurement was performed in a vacuum to avoid the influence of oxygen and moisture. Temperature-dependent in-plane resistivity measurements were performed in a four-arm Lakeshore probe station under vacuum (ca. 10^{-4} Pa). A linear four-contacts method was used to measure σ (ref. [21]). Gold electrodes were evaporated for the contacts. Electrical measurement was carried out using a Keithley 4200 SCS parameter analyser. σ was calculated from the current (I) and voltage (V) data according to the equation $\sigma = (I/V) \times (l/A)$, where A is the cross-sectional area of the conductor ($A = a \times d$). Parameters l, a and d are the voltage probe's distance, and the sample width and thickness, respectively.

Chemical stability test. We took the stability test in NH_4OH as an example. As-synthesized samples (~100 mg) were suspended in 15 ml of a saturated NH_4OH solution and then heated to 100 °C for 24 h. Afterwards, the sample was further washed with water and acetone. All the samples were subsequently treated by typical activation procedures mentioned previously. After being dried under vacuum for 6 h, the sample was degassed on the ASAP2420 adsorption system for 5 h at 100 °C. These samples were then measured for N_2 sorption at 77 K. Afterwards, all the samples were characterized by PXRD. We also checked the stability of the HAB MOFs in 1 M HCl. The PXRD did not show a notable change.

To demonstrate that partial etching of the framework does not happen during the synthesis, we additionally measured the mass change before and after the stability test. For each condition, we started with ~50 mg of sample. After the stability test, the samples were fully washed with water and acetone to remove the entrapped chemical species. A centrifuge was used for the washing process to avoid mass loss during the sample transfer. During the washing, the processed the supernatant is colourless, which is evidence of framework intactness during stability test because both the ligand and metal species are soluble in water. The fully washed samples were finally dried in a vacuum oven. Eventually, the mass change for each sample was around 1.0–1.5 mg, which is the result of the inevitable mass loss during washing because of the extremely small particle size of our MOF product.

Preparation the Ni-HAB and Cu-HAB composite electrode film. To prepare composite free-standing electrodes, first we ground together in an agate mortar and in 2 ml of ethanol (200 proof, Sigma-Aldrich) 20 mg of HAB MOF powder, 1.85 mg of PTFE binder solution (60 wt% in H_2O (Aldrich)) and 1.1 mg of carbon black powder until a homogenous slurry was formed. Then, once the ethanol had evaporated at room temperature, the dried slurry was transferred onto a glass surface with a few ethanol drops added and then subjected to mechanical processing: repeated kneading with a stainless-steel spatula until the powder particles started to stick together before finally being rolled into a free-standing film. The resulting electrodes used for the initial evaluation of the materials' electrochemical performances contained 90 wt% HAB MOF, 5 wt% PTFE and 5 wt% carbon black.

Ni-HAB electrode pellet preparation. To prepare pellets, neat as-synthesized Ni-HAB powders were cold pressed isostatically using commercial pressing equipment (MTI Corporation).

Activated carbon counter electrodes. Activated carbon film electrodes were prepared following the same procedure as for the HAB MOF composite electrodes, but without any conductive additive. The resulting electrode composition was 95 wt% of YEC-200 activated carbon (Yihuan Carbon) and 5 wt% of the PTFE. The electrodes had a mass density per unit area of 10–25 mg cm^{-2}.

Electrochemical measurements. All electrochemical measurements (cyclic voltammetry, galvanostatic cycling and EIS) were performed using a VSP potentiostat (Biologic) in 1 M KOH solution (99.98% (Acros Organics)) in PFA three-electrode Swagelok cells. HAB MOF served as the working electrode, overcapacitive activated carbon film ($m_{AC} > 10\, m_{HAB\,MOF}$) was used as the counter electrode and Ag/AgCl in 1 M KCl was used as a reference to control precisely the electrochemical potentials.

Cyclic voltammetry was performed using scan rates from 0.2 to 100 mV s^{-1}. EIS was performed at an open-circuit potential with a 10 mV amplitude between 50 and 200 kHz. Galvanostatic cycling was performed at 1 and 10 A g^{-1} with potential limits selected specifically for each HAB MOF: from −0.75 to −0.25 V vs Ag/AgCl for Ni-HAB and from −0.55 to −0.1 V vs Ag/AgCl for Ci-HIB.

The capacitance was calculated from cyclic voltammetry or galvanostatic cycling by integration of the current with respect to time: $C = \int |i| \mathrm{d}t m^{-1} V^{-1}$, where C is the gravimetric capacitance (F g^{-1}), i is the current (A), m is the material weight (g) and V is the potential window (V). To obtain the volumetric and areal capacitances, the gravimetric capacitance was multiplied by the volumetric (g cm^{-3}) or areal (g cm^{-2}) density of electrode.

Data availability. The data that support the plots within this paper and other findings of this study are available from the corresponding author on reasonable request.

Received: 13 June 2017; Accepted: 23 October 2017;
Published online: 1 January 2018

References

1. Huang, P. et al. On-chip and freestanding elastic carbon films for micro-supercapacitors. *Science* **351**, 691–695 (2016).
2. Beidaghi, M. & Gogotsi, Y. Capacitive energy storage in micro-scale devices: recent advances in design and fabrication of micro-supercapacitors. *Energy Environ. Sci.* **7**, 867–884 (2014).
3. Simon, P. & Gogotsi, Y. Materials for electrochemical capacitors. *Nat. Mater.* **7**, 845–854 (2008).
4. Xu, Y. et al. Holey graphene frameworks for highly efficient capacitive energy storage. *Nat. Commun.* **5**, 4554 (2014).
5. Zhu, Y. et al. Carbon-based supercapacitors produced by activation of graphene. *Science* **332**, 1537–1541 (2011).
6. Zhao, X. et al. Incorporation of manganese dioxide within ultraporous activated graphene for high-performance electrochemical capacitors. *ACS Nano* **6**, 5404–5412 (2012).
7. Snook, G. A., Kao, P. & Best, A. S. Conducting-polymer-based supercapacitor devices and electrodes. *J. Power Sources* **196**, 1–12 (2011).
8. Kyerematen, N. A., Brousse, T. & Pech, D. Microsupercapacitors as miniaturized energy-storage components for on-chip electronics. *Nat. Nanotech.* **12**, 7–15 (2016).
9. Gogotsi, Y. & Simon, P. True performance metrics in electrochemical energy storage. *Science* **334**, 917–918 (2011).
10. Zhou, H.-C., Long, J. R. & Yaghi, O. M. Introduction to metal–organic frameworks. *Chem. Rev.* **112**, 673–674 (2012).
11. Wang, L. et al. Metal–organic frameworks for energy storage: batteries and supercapacitors. *Coord. Chem. Rev.* **307**, 361–381 (2016).
12. Mulzer, C. R. et al. Superior charge storage and power density of a conducting polymer-modified covalent organic framework. *ACS Cent. Sci.* **2**, 667–673 (2016).
13. Sheberla, D. et al. Conductive MOF electrodes for stable supercapacitors with high areal capacitance. *Nat. Mater.* **16**, 220–224 (2017).
14. Zhang, Z. & Awaga, K. Redox-active metal–organic frameworks as electrode materials for batteries. *MRS Bull.* **41**, 883–889 (2016).

15. Dincă, M. & Léonard, F. Metal–organic frameworks for electronics and photonics. *MRS Bull.* **41**, 854–857 (2016).
16. Wang, Q., Yan, J. & Fan, Z. Carbon materials for high volumetric performance supercapacitors: design, progress, challenges and opportunities. *Energy Environ. Sci.* **9**, 729–762 (2016).
17. Sun, L., Campbell, M. G. & Dincă, M. Electrically conductive porous metal–organic frameworks. *Angew. Chem. Int. Ed.* **55**, 3566–3579 (2016).
18. Sheberla, D. et al. High electrical conductivity in Ni_3(2,3,6,7,10,11-hexaiminotriphenylene)$_2$, a semiconducting metal–organic graphene analogue. *J. Am. Chem. Soc.* **136**, 8859–8862 (2014).
19. Kambe, T. et al. Redox control and high conductivity of nickel bis(dithiolene) complex π-nanosheet: a potential organic two-dimensional topological insulator. *J. Am. Chem. Soc.* **136**, 14357–14360 (2014).
20. Huang, X. et al. A two-dimensional π–d conjugated coordination polymer with extremely high electrical conductivity and ambipolar transport behaviour. *Nat. Commun.* **6**, 7408 (2015).
21. Givaja, G., Amo-Ochoa, P., Gomez-Garcia, C. J. & Zamora, F. Electrical conductive coordination polymers. *Chem. Soc. Rev.* **41**, 115–147 (2012).
22. Mahmood, J., Kim, D., Jeon, I.-Y., Lah, M. S. & Baek, J.-B. Scalable synthesis of pure and stable hexaaminobenzene trihydrochloride. *Synlett* **24**, 246–248 (2013).
23. Mahmood, J. et al. Nitrogenated holey two-dimensional structures. *Nat. Commun.* **6**, 6486 (2015).
24. Nandasiri, M. I., Jambovane, S. R., McGrail, B. P., Schaef, H. T. & Nune, S. K. Adsorption, separation, and catalytic properties of densified metal–organic frameworks. *Coord. Chem. Rev.* **311**, 38–52 (2016).
25. Kobayashi, Y., Jacobs, B., Allendorf, M. D. & Long, J. R. Conductivity, doping, and redox chemistry of a microporous dithiolene-based metal−organic framework. *Chem. Mater.* **22**, 4120–4122 (2010).
26. Hmadeh, M. et al. New porous crystals of extended metal-catecholates. *Chem. Mater.* **24**, 3511–3513 (2012).
27. Campbell, M. G., Sheberla, D., Liu, S. F., Swager, T. M. & Dincă, M. Cu_3(hexaiminotriphenylene)$_2$: an electrically conductive 2D metal–organic framework for chemiresistive sensing. *Angew. Chem. Int. Ed.* **54**, 4349–4352 (2015).
28. Wang, K. et al. Pyrazolate-based porphyrinic metal–organic framework with extraordinary base-resistance. *J. Am. Chem. Soc.* **138**, 914–919 (2016).
29. Conway, B. *Electrochemical Supercapacitors: Scientific Fundamentals and Technological Applications* (Kluwer Academic/Plenum, New York, 1999).
30. Augustyn, V. et al. High-rate electrochemical energy storage through Li^+ intercalation pseudocapacitance. *Nat. Mater.* **12**, 518–522 (2013).
31. Ghidiu, M., Lukatskaya, M. R., Zhao, M.-Q., Gogotsi, Y. & Barsoum, M. W. Conductive two-dimensional titanium carbide 'clay' with high volumetric capacitance. *Nature* **516**, 78–81 (2014).
32. Wolff, J. J. et al. Hexaaminobenzene derivatives: synthesis and unusual oxidation behavior. *J. Org. Chem.* **66**, 2769–2777 (2001).
33. Herebian, D., Bothe, E., Neese, F., Weyhermüller, T. & Wieghardt, K. Molecular and electronic structures of bis-(*o*-diiminobenzosemiquinonato) metal(II) complexes (Ni, Pd, Pt), their monocations and -anions, and of dimeric dications containing weak metal−metal bonds. *J. Am. Chem. Soc.* **125**, 9116–9128 (2003).
34. Yu, Z., Tetard, L., Zhai, L. & Thomas, J. Supercapacitor electrode materials: nanostructures from 0 to 3 dimensions. *Energy Environ. Sci.* **8**, 702–730 (2015).
35. Lukatskaya, M. R., Dunn, B. & Gogotsi, Y. Multidimensional materials and device architectures for future hybrid energy storage. *Nat. Commun.* **7**, 12647 (2016).
36. Lin, T. et al. Nitrogen-doped mesoporous carbon of extraordinary capacitance for electrochemical energy storage. *Science* **350**, 1508–1513 (2015).
37. Xu, Y. et al. A metal-free supercapacitor electrode material with a record high volumetric capacitance over 800 F cm^{-3}. *Adv. Mater.* **27**, 8082–8087 (2015).
38. Acerce, M., Voiry, D. & Chhowalla, M. Metallic 1T phase MoS_2 nanosheets as supercapacitor electrode materials. *Nat. Nanotech.* **10**, 313–318 (2015).
39. Yang, X., Cheng, C., Wang, Y., Qiu, L. & Li, D. Liquid-mediated dense integration of graphene materials for compact capacitive energy storage. *Science* **341**, 534–537 (2013).
40. Sarkisov, L. & Harrison, A. Computational structure characterisation tools in application to ordered and disordered porous materials. *Mol. Simul.* **37**, 1248–1257 (2011).
41. Zhu, Y. et al. Unravelling surface and interfacial structures of a metal–organic framework by transmission electron microscopy. *Nat. Mater.* **16**, 532–536 (2017).

Acknowledgements

This work was supported by Stanford School of Engineering SUNCAT seed funding. Part of this work was funded by the Office of Energy Efficiency and Renewable Energy (EERE), US Department of Energy, under Battery Materials Research Program. We gratefully acknowledge support from the US Department of Energy, Office of Sciences, Office of Basic Energy Sciences to the SUNCAT Center for Interface Science and Catalysis. J.P. acknowledges supported by the Dreyfus Foundation Environmental Postdoc Fellowship. L.S. gratefully acknowledges support from Kodak Graduate Fellowship. The structure characterization by TEM and PXRD was supported by the Knut & Alice Wallenberg Foundation through project grant 3DEM-NATUR and the Swedish Research Council (VR) through the MATsynCELL project of the Röntgen-Ångström Cluster. Use of the SSRL, SLAC National Accelerator Laboratory, is supported by the US Department of Energy, Office of Science, Office of Basic Energy Sciences under Contract No. DE-AC02-76SF00515.

Author contributions

D.F., T.L., M.R.L and J.P. designed and synthesized the HAB MOFs. M.R.L. performed the electrochemical characterization and analysis. D.F. performed the gas absorption measurements. T.L. measured the photophysical and electrical properties and performed the structure modelling. Z.H. and X.Z. performed the TEM measurements and structure refinement. M.L. performed the SEM imaging. L.S. performed the GIXD experiments and analysis. S.C. performed the XPS characterization. A.A.Y. performed the synchrotron powder X-ray measurements. A.K., J.X. and K.F. performed the DFT calculations. D.F., T.L., M.R.L., J.B.T., Y.C. and Z.B. co-wrote the paper. All the authors discussed the results and commented on the manuscript.

Competing interests

The authors declare no competing financial interests.

Additional information

Supplementary information is available for this paper at https://doi.org/10.1038/s41560-017-0044-5.

Reprints and permissions information is available at www.nature.com/reprints.

Correspondence and requests for materials should be addressed to Z.B.

Publisher's note: Springer Nature remains neutral with regard to jurisdictional claims in published maps and institutional affiliations.